BeBeC-2022-S05

TUNING OF THE FUNCTIONAL BEAMFORMING RESOLUTION FOR WIND TUNNEL MEASUREMENTS

Gianmarco Battista[1], Paolo Chiariotti[1] and Paolo Castellini[2]
[1]Università Politecnica delle Marche
Via Brecce Bianche, 60121 Ancona, Italy
[2]Politecnico di Milano

Abstract

Conventional Frequency Domain Beamforming (CB) is characterised by the frequency dependency of the mainlobe width and by the presence of sidelobes that limit its dynamic range. Functional Beamforming (FB) has been introduced with the aim to overcome these limitations, narrowing the mainlobe and reducing the sidelobe levels. This paper introduces a strategy to obtain a beamformer with a target mainlobe width that is constant over a desired frequency range. The idea is to properly adjust the Functional Beamforming order ν, frequency by frequency, to preserve the mainlobe width. A tuning procedure of the order ν is presented and applied to a typical wind tunnel setup. A detailed analysis of the dependency "order ν versus frequency" is discussed and a general formula describing this dependency is provided. Finally, the effectiveness of the proposed approach is shown both on simulated and experimental test cases.

1 INTRODUCTION

Phased microphone array measurements are an effective tool for studying noise sources, both in industrial and research contexts. In fact, this technology, combined with acoustic source mapping techniques, makes it possible to estimate the position and the strength of noise sources. The applications range from wind–tunnel experiments, where the aeroacoustic noise of airfoil or aircraft models can be studied ([7, 25]), to rotating machinery, like small fans [3, 16] or wind turbines [9, 20]. Chiariotti et al. [10] provided a review of the various algorithms and applications associated to phased array measurements, while Merino-Martinez et al. in [18] provided a review targeted to aeroacoustic applications. The literature provides several classifications of these methods, depending on the calculation domain (commonly time or frequency) or on the approach adopted to solve the inverse acoustic problem. A unified formalism for frequency domain methods was proposed by Leclère et al. in [17]. Normally,

these methods rely on the definition of a Region Of Interest (ROI), that is discretized with a set of potential elementary sources (plane waves, monopoles, dipoles etc.), and the assumption of an acoustic propagation model from sources to microphones.

Conventional Frequency Domain Beamforming (CB) [23] is known to produce maps contaminated by the Point Spread Function (PSF), i.e. the array spatial response. The PSF is characterised by the mainlobe (global maximum) representing the source, and by several artefacts (local maxima), named sidelobes or ghost images, that limits the useful dynamic range of the map. The mainlobe width (MLW) is related to the ability of a beamformer in distinguishing neighboured sources. Functional Beamforming (FB), developed by Dougherty [12], is an improvement of CB in this sense, since makes it possible to narrow the mainlobe and to lower the sidelobes by simply acting on a single parameter, i.e. the beamformer order ν.

One of the typical issues with beamformers like CB or FB is that the MLW, hence the spatial resolution, is frequency dependant. The separation of different sound sources is of great importance when it comes to the interpretation of results, especially in the identification of aeroacoustic sources in wind tunnel testing. Therefore, it is desirable to have the same MLW for the whole frequency range of interest. In [4], Bahr and Lockard pursued the objective of fixed MLW with CB across a certain frequency range by designing different radial shading scheme for microphone arrays. In this paper, a different approach in pursued. The strategy proposed here is based on the adjustment of the order ν, frequency by frequency, to control the FB spatial resolution. In such way, it is possible to match a target MLW and counteract its increment towards low frequencies. The effectiveness of this strategy is demonstrated on a typical wind tunnel experiment for aeroacoustic source mapping.

2 EXAMPLE TEST CASE: DLR1

The methodology presented in this paper is demonstrated on the Array Methods Experimental Benchmark dataset DLR1 [2]. These measurements were conducted at the cryogenic wind tunnel at the DLR Cologne site, Kryo-Kanal Koeln (DNW-KKK) which is a continuous-flow low-speed wind tunnel with a 2.4 m $\times$ 2.4 m closed-wall test section. In [1], further details on the wind tunnel and the model are provided. In these experiments, the test section hosts a Dornier 728 half-model (scale 1:9.24). The benchmark provides data for 135 microphones which form an array of a 1.046 m diameter. Both the model and the array are depicted in Fig. 1. The measurement used in this paper is the run named as *"dp22"*, that corresponds to an angle of attack of 3°, a Mach number of 0.15 and a temperature of 286.12 K. The speed of sound is 345.07 m/s. A simple scheme of the Dornier 728 half-model is shown in Fig. 2, together with the ROI discretised with a grid of 0.01 m step. Depending on the angle of attack used for the test, the grid is properly rotated to "adhere" on the actual model position as explained in [2]. After the rotation, the mean distance between the array plane and the calculation plane is approximately 1.12 m. The distance between the leading and the trailing edges varies from about 0.13 m to 0.50 m, while the average distance between the leading edge slat tracks is about 0.11 m. These are some potential noise source locations, hence their mutual distances establish the spatial resolution requirements for the source imaging technique.

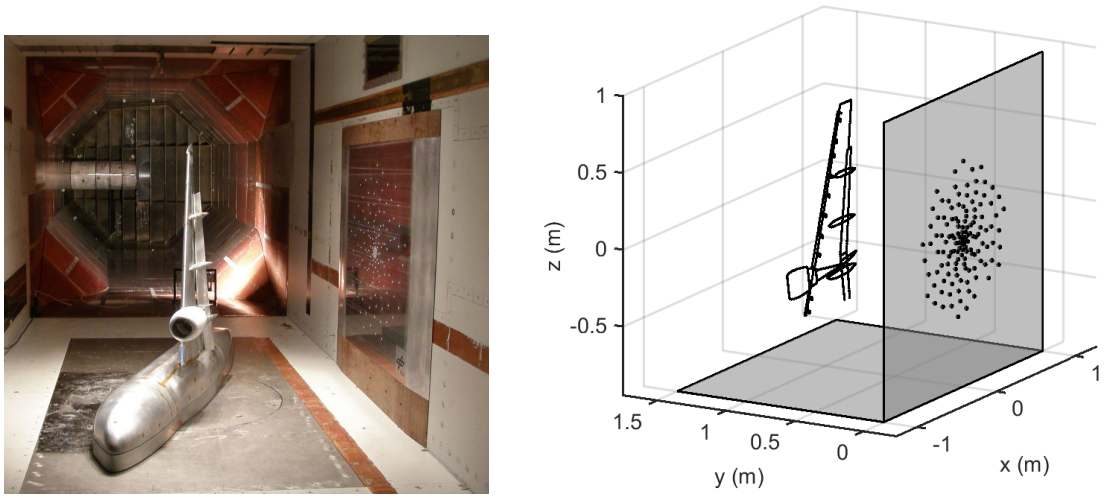

Figure 1: Photo and scheme of measurement setup for DLR1 benchmark dataset.

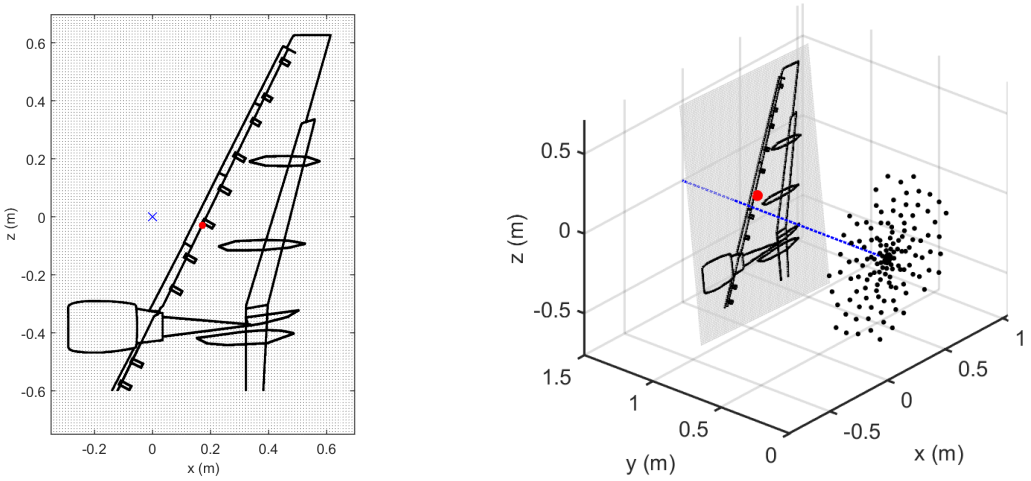

Figure 2: Dornier 728 half-model details and Region Of Interest grid (in grey) for beamforming maps. The grid resolution is 0.01 m. The red dot represent the grid centre and the target position $\mathbf{x}_{tgt}$ for the FB resolution tuning. The blue dotted line indicates the array longitudinal axis.

3 METHODOLOGY

3.1 Functional Beamforming

The sound pressure signals recorded by each of the M microphones in the array are processed to obtain the Cross-Spectral-Matrix (CSM) $\mathbf{P}$ for each frequency as

$$\mathbf{P} = \mathbb{E}\left\{\mathbf{p}\mathbf{p}^{\mathrm{H}}\right\}, \tag{1}$$

where $\mathbf{p}$ is the M-by-1 vector containing the complex pressure on each microphone, $\mathbb{E}\{\}$ represents the expectation operator and $^{\mathrm{H}}$ denotes the conjugate transpose. The Welch's method is commonly adopted for CSM estimation [24]. A target ROI is defined, representing the region to scan with the beamformer, and then it is covered by a set of N potential monopole sources that are the focus points. The frequency domain acoustic propagation is modelled by means of complex coefficients, $g_{n,m}$, accounting for the wave propagation from the n-th source at $\mathbf{x}_n$ to the m-th microphone located at $\mathbf{y}_m$. These coefficients are collected in M-by-1 vectors $\mathbf{g}_n$, accounting for the wave propagation from a single potential source to all microphones. Free-field propagation of a monopole source can be expressed in "pressure-to-pressure" formulation [8, 21] as:

$$g_{n,m}(\mathbf{x}_n, \mathbf{y}_m, \mathbf{y}_0) = \frac{r_{n,0}}{r_{n,m}} \mathrm{e}^{\mathrm{i}k(r_{n,m}-r_{n,0})}, \tag{2}$$

where k is the wavenumber and te symbol "i" indicates the imaginary unit. This acoustic transfer function relates the pressure caused by a monopole (located in $\mathbf{x}_n$) at the reference point $\mathbf{y}_0$, that is usually located at the geometric centre of the array, to the one perceived by a microphone at $\mathbf{y}_m$. The terms $r_{n,0} = \|\mathbf{x}_n - \mathbf{y}_0\|_2$ and $r_{n,m} = \|\mathbf{x}_n - \mathbf{y}_m\|_2$ are the propagation distances from point source respectively to reference point and to each microphone. In presence of convective effects [22], as in the application described in Section 2, or in presence of rotating flow [15], the geometric distances are replaced by those corresponding to the actual wave travel times.

The array can be focused on a potential source using the steering vector. Among the four different steering vector formulations studied by Sarradj in [21], the *formulation IV* has been adopted in this work, which provides the correct source location, at cost of small systematic error on source level. For each focusing point, this type of steering vector is defined as

$$\mathbf{h}_n = \frac{1}{\sqrt{N}} \frac{\mathbf{g}_n}{\sqrt{\mathbf{g}_n^{\mathrm{H}}\mathbf{g}_n}}. \tag{3}$$

The Functional Beamforming output is calculated using the following expression:

$$b_n(\nu) = \left[\mathbf{h}_n^{\mathrm{H}} \mathbf{P}^{\frac{1}{\nu}} \mathbf{h}_n\right]^{\nu}, \tag{4}$$

where the parameter ν is the beamformer order and $\mathbf{h}_n$ is the steering vector defined in Eq. 3. Equation 4 requires the calculation of the ν-th root of the CSM, that can be calculated by means of eigenvalue decomposition:

$$\mathbf{P}^{\frac{1}{\nu}} = \mathbf{U}\Sigma^{\frac{1}{\nu}}\mathbf{U}^{\mathrm{H}}. \tag{5}$$

The diagonal matrix $\Sigma^{\frac{1}{\nu}} = diag([\sigma_1^{\frac{1}{\nu}}, \sigma_2^{\frac{1}{\nu}}, \ldots, \sigma_M^{\frac{1}{\nu}}])$ contains the M eigenvalues of $\mathbf{P}$, while $\mathbf{U}$ is a unitary matrix whose columns are the eigenvectors. The operator $diag(\cdot)$ indicates a square diagonal matrix having on its main diagonal the elements of the vector given as argument. For $\nu = 1$, FB falls back to CB.

An important assumption at the basis of FB is that the peak value of th PSF is equal (or at least close) to 1 at the source location, thus meaning that the steering vector at the source location matches with the actual source propagation. If this condition holds, an increment of the order ν causes a reduction of the sidelobe level, while the peak of the PSF remains unaltered. In real applications, there is no perfect match between the computed steering vectors and the measured complex pressures, therefore, an upper limit to the value of ν exists. A simple practice to find this limit is to increase the exponent ν until the peaks corresponding to true sources begin to fall off significantly. A detailed analysis of this aspect is described in [5], where the propagation model errors are indicated as the main cause. In order to exploit high values of ν, Dougherty [12] highlights the importance of the an accurate array calibration and the use of a sufficiently fine discretization of the mapping area. In [19], FB maps are scaled to match the peak level with the peak level of CB map, hence compensating the artefact level reduction due to model errors, assuming that CB provides accurate levels. Another aspect to consider is the presence of uncorrelated noise on the CSM diagonal. A common practice to cope with this problem with CB is to set the CSM diagonal entries to zero. However, this practice is not recommended with FB. This limitation can be overcome by adopting array denoising techniques such as the diagonal denoising proposed by Hald [14], the probabilistic approach proposed by Dinsenmeyer et al. [11] or the spherical harmonics decomposition for spherical arrays developed by Battista et al. [6].

3.2 Characterisation of mainlobe width

The spatial resolution limit of CB is commonly assessed with the Rayleigh criterion [13], which relies on the hypotheses that the pressure field is sampled by a continuous circular aperture and the beamformer focusing is at infinite distance, i.e. plane waves are assumed. However, these assumptions are hardly met in experimental applications, therefore, the Rayleigh criterion provides only an approximation of the CB resolution. In fact, the actual number of microphones (i.e. spatial sampling points) is limited and spherical waves are usually considered, being the array focalization at finite distance. For these reasons, an accurate knowledge of MLW requires a ”measurement” for each particular array design and source position. The same lack of knowledge occurs as FB resolution limit is concerned. The MLW is generally indicated as the extension of the region around the PSF main peak where the array response decays of 3 dB. Figure 3 provides an example of PSF and its MLW. For the scope of this paper, it is crucial to define a systematic method to measure the actual beam width for a generic planar array that is also compatible with FB. Considering the PSF calculated on a plane parallel to the array, the mainlobe shape is influenced by two main factors: the microphone arrangement and the source position with respect to the array. For the spiral-like microphone layout adopted in this application (Fig. 1), the mainlobe is almost axis-symmetric and its area can be well approximated by a circle, when a point source on the array longitudinal axis is

considered. However, if the source is positioned off-axis, the mainlobe results distorted, having an ellipsoidal shape.

In this work, the measurement of MLW is performed considering the PSF on a circumference centred on the point source location, independently on the actual mainlobe shape. To gather the mainlobe radius R_{ML}, the metric adopted is the mean value of the PSF calculated on the aforementioned circumference. Therefore, the actual mainlobe radius is given by the circumference having the mean PSF value equal to -3 dB. This circle is named here *"equivalent mainlobe circumference"*. The MLW is two times the mainlobe radius. Figure 4 shows an example for both on-axis and off-axis source. The green circle is the equivalent mainlobe circumference representing the MLW extension obtained with this criterion. The source on array axis produces a PSF profile on the circumference having small fluctuations with respect to the mean value of -3 dB, while the off-axis source produces a distorted lobe, hence greater fluctuations of the PSF profile. This criterion is fully compatible with FB, therefore it is adopted as method for the characterisation of the mainlobe size in terms of R_{ML} for the wind tunnel application described in Section 2.

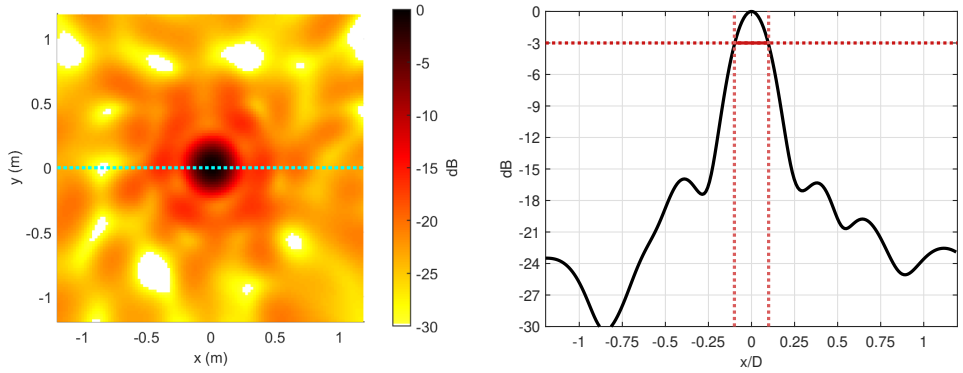

Figure 3: Left: Example of PSF on a plane for a source on the array longitudinal axis. Right: PSF profile on the horizontal cut of the plane indicated by the dotted cyan line in the left figure. The MLW is delimited by the two dotted vertical red lines.

The mainlobe characterisation is done here by considering the setup shown in Fig. 2, where the ROI is depicted with respect to the array. The point source used to render the PSF and measure the actual MLW is positioned on the centre of this region, thus resulting to be slightly off-axis. For the following analysis, the frequencies are expressed in non-dimensional form as Helmholtz numbers $He = f\,D/c$, with f being the frequency, D the array diameter and c the speed of sound. The analysis of MLW is conducted as function of two parameters: Helmholtz number and order ν. The frequency ranges from $He = 4$ ($\approx$1.3 kHz) to $He = 100$ ($\approx$33 kHz), while the FB order ν ranges from 1 to 100. Both parameters are varied on a logarithmic equally spaced grid with 40 values, thus having 1600 He-ν pairs. Figure 5 shows the measured MLW both in linear and logarithmic scale. The mainlobe radius follows an expected trend, i.e. it is inversely proportional to the frequency and to the order. In logarithmic scale, all the values of R_{ML} seem to be arranged almost on a plane. From this consideration, a possible model for the

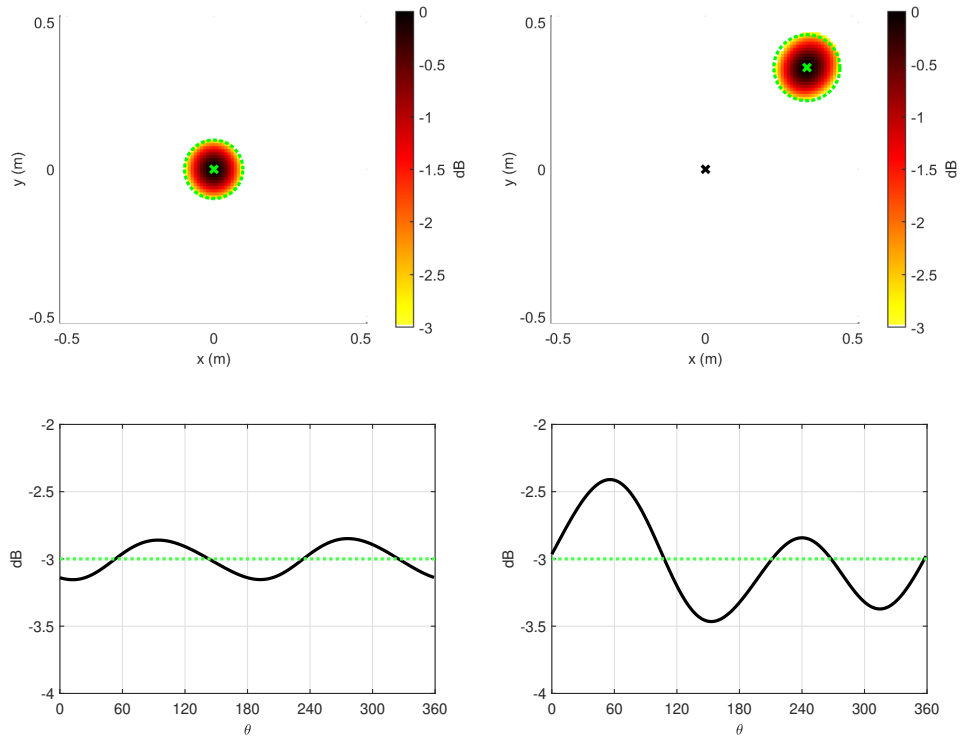

Figure 4: MLW measurement using the mean PSF value on a circumference centred in the exact source location. Top figures shows the PSF on the calculation plane, while bottom figure depicts the PSF profile on the equivalent mainlobe circumference. Left: on axis point source. Right: off-axis point source. The black cross represents the projection of the array longitudinal axis on the mapping plane.

mainlobe radius can be:

$$R_{ML}(He, \nu) = a_0 \cdot He^{a_1} \cdot \nu^{a_2}\,, \tag{6}$$

that can be conveniently rewritten in logarithmic scale as

$$\log(R_{ML}(He, \nu)) = \log(a_0) + a_1 \log(He) + a_2 \log(\nu)\,. \tag{7}$$

In such form the terms $\log(a_0)$, a_1 and a_2 can be estimated from the data adopting a least-squares approach for a multiple linear regression. Using the MATLAB *"fit"* function and the model *"poly11"*, the coefficients are $\log(a_0) = -0.256$, $a_1 = -1.001$ and $a_2 = -0.4612$, with root mean square error of 0.031 m and a determination coefficient $R^2 = 0.999$. If the value of a_1 is absolutely not surprising, what is interesting is the value of a_2 which indicates the precise trend of the MLW with respect to the FB order.

3.3 FB resolution tuning

The choice of target resolution is done in terms of CB MLW by considering a point source in a convenient position $\mathbf{x}_{tgt}$, for instance, on the array axis or in the ROI centre. Given the target

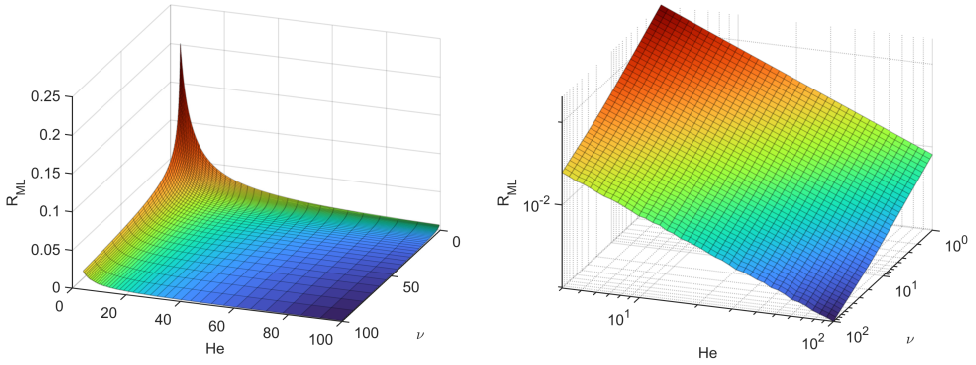

Figure 5: MLW measurements for FB with respect to Helmholtz number (4-100) and order (1-100). Left: linear scale. Right: logarithmic scale.

location, the other parameter to choose is the target mainlobe radius $R_{ML,tgt}$. It is also convenient to define the corresponding Helmholtz number He_{tgt}, that is the frequency for which CB returns the a mainlobe with the target radius. The objective of the next steps is to assess the proper order value $\bar{\nu}$ to ensure the target mainlobe radius for each frequency below He_{tgt}. Once the reference source position is fixed, the value of $\bar{\nu}$ is dependent on the target mainlobe radius $R_{ML,tgt}$ (or equivalently on He_{tgt}) and the frequency of analysis He. Consider Eq. 7, that can be modified in the following form:

$$\log\left(\frac{R_{ML}}{R_{ML,tgt}}\right) = a_1 \log\left(\frac{He}{He_{tgt}}\right) + a_2 \log(\nu)\,, \tag{8}$$

where both the mainlobe radii and the Helmholtz numbers are normalised by their target values. In this form, $\log(a_0)$ vanishes, since $\nu = 1$ by definition when $R_{ML} = R_{ML,tgt}$ and $He = He_{tgt}$. In other words, when both mainlobe radius and frequency are normalised by the target values no offset is left. The condition of constant MLW is imposed by forcing $R_{ML} = R_{ML,tgt}$ for any frequency and order. The resulting equation can be rearranged to obtain:

$$\log(\bar{\nu}) = -\frac{a_1}{a_2} \log\left(\frac{He}{He_{tgt}}\right) = K \log\left(\frac{He}{He_{tgt}}\right)\,. \tag{9}$$

In this form, a single coefficient K is sufficient to define an explicit expression for $\bar{\nu}$ as function of He and He_{tgt}. The steps for its estimation can be summarized as:

1. define the target source position $\mathbf{x}_{tgt}$;
2. define the target mainlobe radius $R_{ML,tgt}$ and consequently He_{tgt};
3. measure the mainlobe radius R_{ML} for a sufficiently large set of pairs (He, ν), with $He \leq He_{tgt}$ and $\nu \geq 1$, using the method described in Section 3.2;
4. fit the measured data from the previous step, in the normalised form of Eq. 8, to estimate the coefficients a_1 and a_2 with a polynomial surface of the first order;

5. calculate the coefficient K from the values a_1 and a_2 as in Eq.9.

Once K is estimated, the explicit expression to "tune" the order $\bar{\nu}$ is:

$$\bar{\nu} = \left(\frac{He}{He_{tgt}} \right)^K . \tag{10}$$

Regarding the data fitting step a further point needs to be discussed. After the MLW measurements, the data for fitting is prepared by normalising the radii and the Helmholtz numbers by their corresponding target values, thus having the data in the form of Eq. 8. The estimation of a_1 and a_2 is done with a first degree polynomial surface adopting, for example, a Least-Squares Fitting approach, where the independent variables are He/He_{tgt} and ν. However, the normalization of the frequencies and the radii may not be sufficient to ensure that the constant term of the polynomial fitting is exactly equal to zero (corresponding to $\log(a_0)$). For this reason, this term is forced to zero in the fitting stage, since the value of $\bar{\nu}$ is equal to 1 at target conditions.

For the wind tunnel application described in Section 2, the chosen target source position $\mathbf{x}_{tgt}$ is the centre of the calculation grid depicted in Fig. 2. The target mainlobe radius $R_{ML,tgt}$ is set at 0.01 m. In Fig. 7 the mainlobe radius of CB versus the Helmholtz number is shown. The target lobe radius corresponds to $He_{tgt} = 80$ (approximately 26.4 kHz). The value of K is calculated by means of the tuning procedure above described. The characterisation of MLW is performed on a 40-by-40 grid of He-ν pairs. The Helmholtz number ranges from 8 to 80, while the order ranges from 1 to 100. The values are evenly spaced on logarithmic scale. The outcome of these calculation provides the data for the fitting. This is performed with the MATLAB *"fit"* function, using the model *"poly11"*, where the constant term is forced to zero. The outcome is $a_1 = -0.9980$ and $a_2 = -0.4919$ with $R^2 > 0.99$ and a root mean square error of 0.0070 m. The resulting coefficient is $K = 2.0288$ that leads to the exponent curve depicted in Fig. 7, where the value is fixed to 1 for $He \geq He_{tgt}$. Figure 6 shows that the residuals of the fitting are not randomly distributed and suggest a more complex behaviour of R_{ML}. Therefore, the model of Eq. 6 is only an approximated model.

Two examples are presented here to highlight the differences between CB, standard FB with constant order ($\nu = 10$) and FB with the order $\bar{\nu}(He)$ adjusted for each frequency. In both the examples, the ROI is an horizontal segment parallel to the array and centred on the target source location $\mathbf{x}_{tgt}$. In order to highlight the MLW trend, all the beamformers' outputs are normalised by their maximum for each frequency and the maps are plotted with 3 dB of dynamics. In *Example 1*, a single monopole, placed at the target point location, is mapped (Fig. 8). Both CB and standard FB show the typical frequency dependency of the lobe size, while FB with the tuned order $\bar{\nu}$ returns the same MLW for the whole frequency range considered. In *Example 2*, two monopoles are present in the ROI. These are spaced of 0.1 m and centred on the target source location $\mathbf{x}_{tgt}$. The output of FB with tuned exponent gives a better source separation for a wider frequency range. In fact, for this example, CB and standard FB produce a unique lobe respectively below $He = 20$ and $He = 12$, while this happens only $He < 8$ when the FB order is tuned.

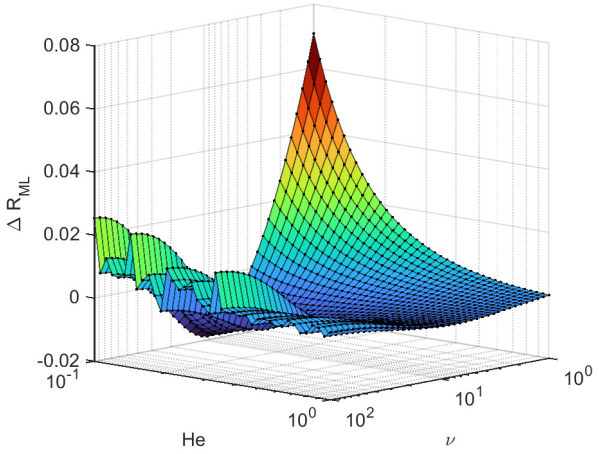

Figure 6: Fitting residuals for the measured mainlobe radii R_{ML} versus frequency and order.

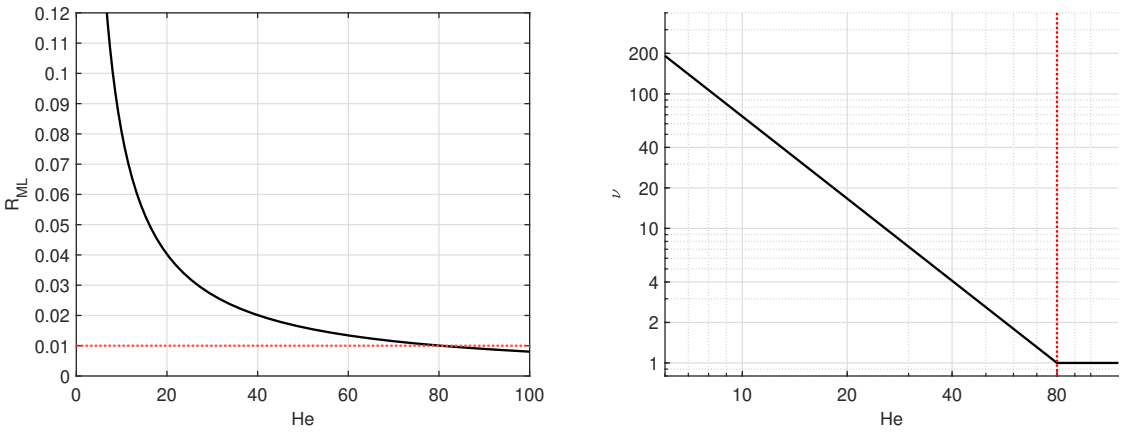

Figure 7: DLR1 array tuning. Left: mainlobe radius of CB for the target point source in the ROI centre. Red dotted line represents the target radius $R_{ML,tgt} = 0.01$ m, corresponding to $He_{tgt} = 80$. Right: tuned FB order $\bar{\nu}$ versus Helmholtz number.

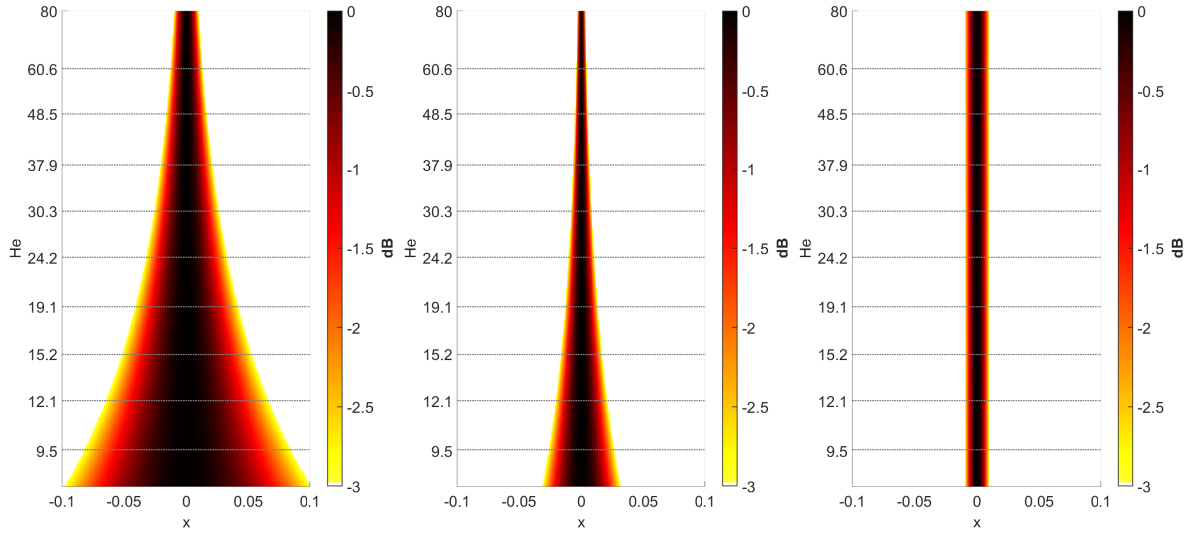

Figure 8: Example 1. Acoustic maps of the target point source on the horizontal 1-dimensional ROI centred in $\mathbf{x}_{tgt}$ and parallel to the array. Horizontal dotted lines are the centre of one-third octave bands from 3.15 kHz to 20 kHz. Left: CB. Centre: FB $\nu = 10$. Right: FB with tuned order $\bar{\nu}$ ($He_{tgt} = 80$, $K = 2.0288$).

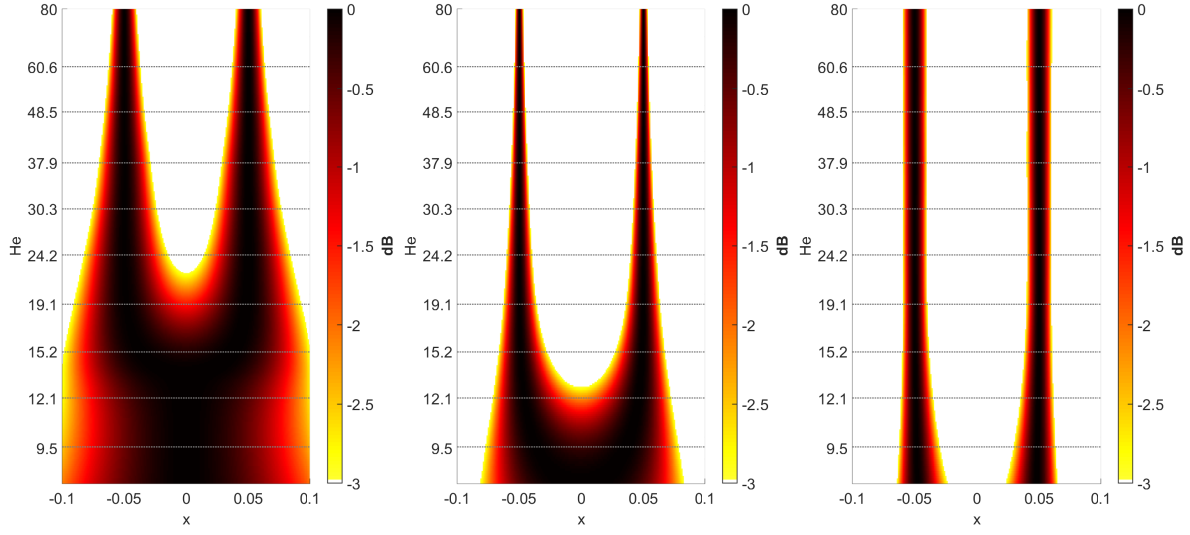

Figure 9: Example 2. Acoustic maps of two point sources spaced of 0.1 m and centred in $\mathbf{x}_{tgt}$. The horizontal 1-dimensional ROI is parallel to the array and centred in on the target point. Horizontal dotted lines are the centre of one-third octave bands from 3.15 kHz to 20 kHz. Left: CB. Centre: FB $\nu = 10$. Right: FB with tuned order $\bar{\nu}$ ($He_{tgt} = 80$, $K = 2.0288$).

4 RESULTS

4.1 Simulated data

Before analysing the experimental case, it is useful to make some experiments with simulated data, hence without background noise and steering vector errors. In this case, the simulation is performed directly in frequency domain using the propagator of Eq. 2. The sources, depicted in Fig. 10 with respect to the model, are simulated on the rotated plane depicted in Fig. 2, that is the same used for the maps with experimental data. Each source produces a level of 60 dB at the array centre for each frequency. The discrete frequency axis used for this simulation has a step of $\Delta He = 0.1$, corresponding to $\Delta f \approx 33$ Hz. On the leading edge, eleven evenly spaced monopoles are placed with about 0.13 m step, corresponding approximately to the edge slat track spacing, while other three sources are placed on the trailing edge flap tip and flap tracks. Figures 11 and 12 show the maps obtained from CB and FB with tuned order for one-third octave bands from 3.15 kHz to 20 kHz. All the maps are depicted with 12 dB of dynamic range. The tuning curve for $\bar{\nu}$ is the one depicted in Fig. 7, obtained with $He_{tgt} = 80$ and $K = 2.0288$. The CB maps show the well known variations of spatial resolution and limits in terms of dynamic range. Contrarily, the tuning procedure of the FB order $\bar{\nu}$ makes it possible to achieve the desired effects, i.e. a constant MLW for a wide frequency range, even with multiple sources, combined with the increment of map dynamics with respect to CB. However, some sources are still not well separated from 5 kHz down, especially those far from the array axis.

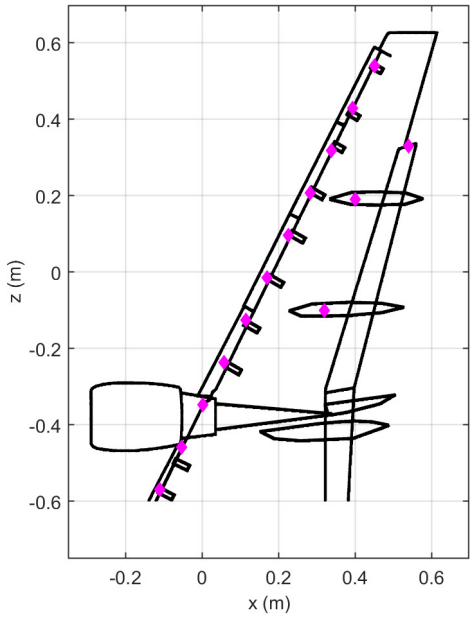

Figure 10: Simulated source locations (magenta diamonds).

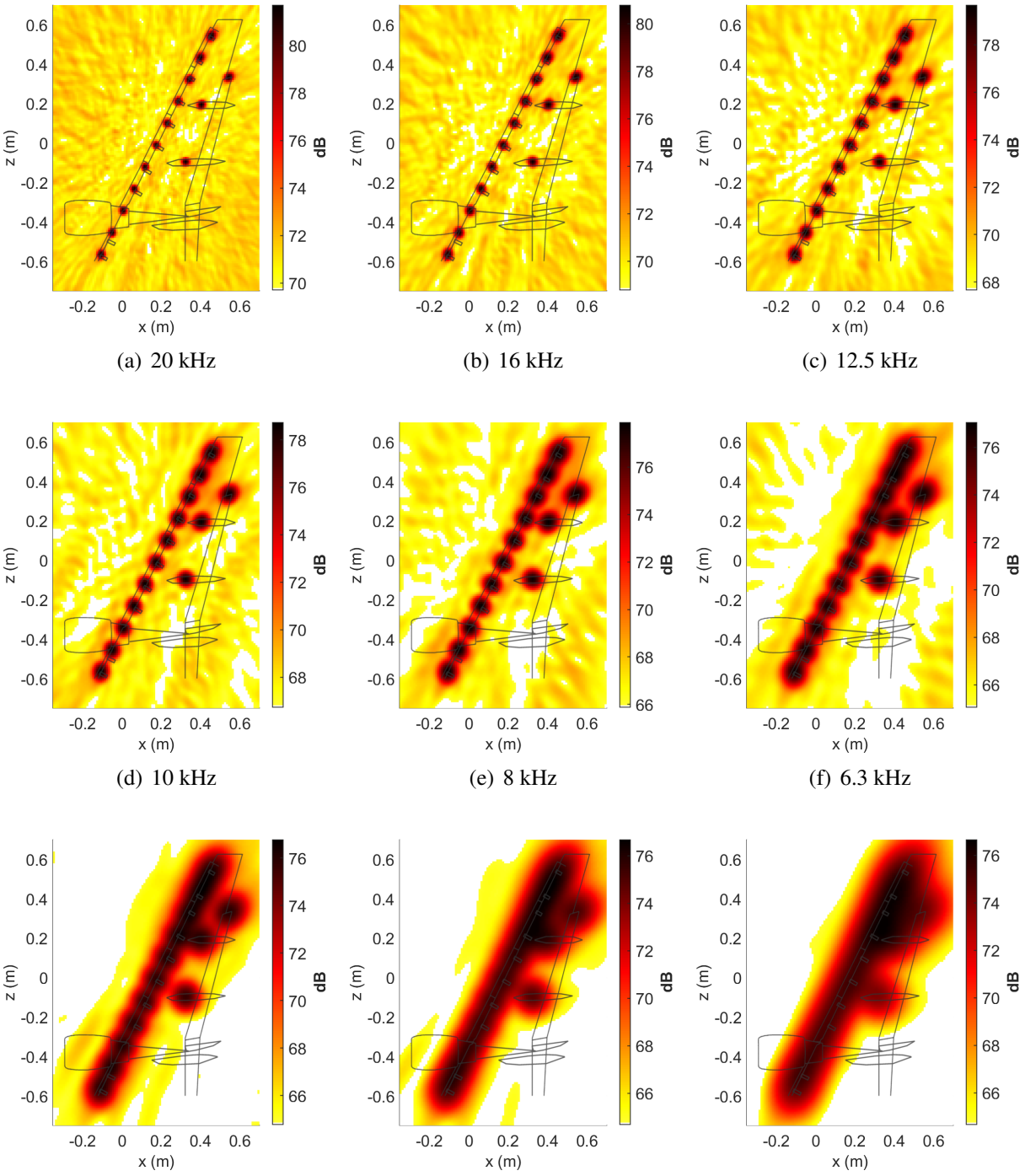

(a) 20 kHz (b) 16 kHz (c) 12.5 kHz

(d) 10 kHz (e) 8 kHz (f) 6.3 kHz

(g) 5 kHz (h) 4 kHz (i) 3.15 kHz

Figure 11: Simulated data. Acoustic maps for different one-third octave bands with Conventional Beamforming.

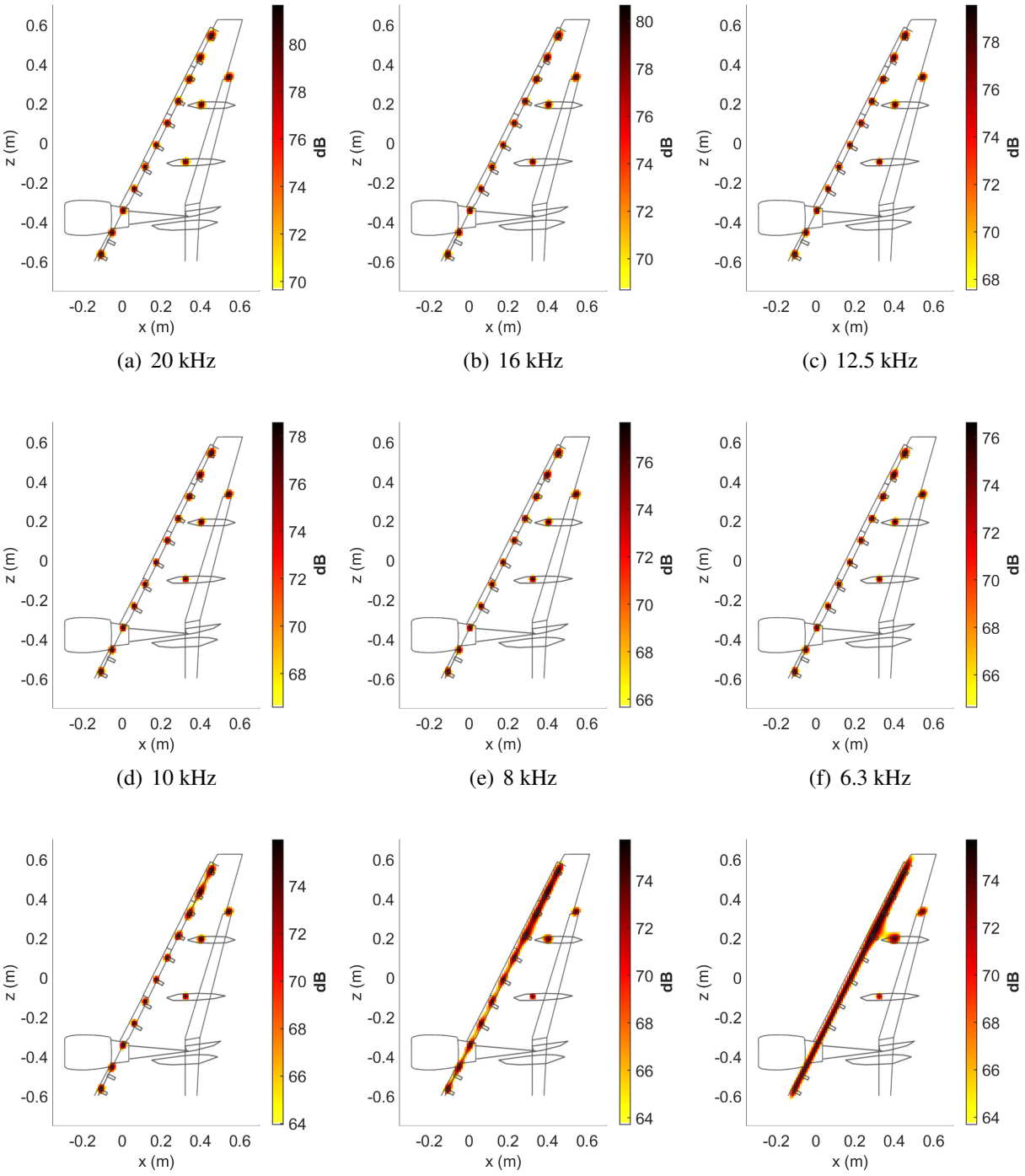

(a) 20 kHz (b) 16 kHz (c) 12.5 kHz

(d) 10 kHz (e) 8 kHz (f) 6.3 kHz

(g) 5 kHz (h) 4 kHz (i) 3.15 kHz

Figure 12: Simulated data. Acoustic maps for different one-third octave bands with Functional Beamforming and tuned order $\bar{\nu}$ ($He_{tgt} = 80$, $K = 2.0288$).

4.2 Experimental data

Before applying the beamformers on the experimental data, two denoising steps are performed on the microphone CSM . The first step reduces the uncorrelated noise on the CSM main diagonal. This procedure ([14]) subtracts the maximum possible power on each CSM diagonal element, while keeping the residual CSM semi-definite positive. The second step is the reduction of background noise that is achieved by means of truncated eigenvalue decomposition. The truncation is done by applying a threshold of 15 dB with respect to the maximum eigenvalue for each frequency. These two denoising steps are performed in order to enhance the map dynamic range and avoid the CSM diagonal removal practice. The maps are calculated on the ROI shown in Fig. 2, using CB and FB. The tuning curve for $\bar{\nu}$ is the same adopted for simulated data. All the maps are depicted with 12 dB of dynamic range. The comparison between CB maps in Fig. 13 and FB maps in Fig. 14 demonstrates the improvements achieved with the tuning of beamforming order. In fact, this strategy effectively counteracts the typical increment of MLW towards low frequencies, thus resulting drastically reduced. In addition, the typical advantages of FB in terms of dynamic range still hold. In fact, the upper limit of 20 kHz band is about $He = 68$, therefore the order utilised is $\bar{\nu} > 1$ for all the maps shown, ranging from 1.39 to 94.4.

5 CONCLUSIONS

In this paper, the tuning of Functional Beamforming order ν has been addressed with the aim of controlling the mainlobe width over a frequency range. The advantage of this approach is twofold. On the one hand the mainlobe size remains constant for a wide frequency range, while, on the other hand, the acoustic map gains the well known benefits of Functional Beamforming in terms of dynamic range. To achieve this result, it is crucial to have a detailed characterisation of the relation existing, for a particular array, between frequency, order ν and mainlobe width. In this work, a method to measure the mainlobe size is defined by assuming an axial-symmetric lobe, thus having as output the radius of an equivalent mainlobe circumference. The data generated in the characterisation step are used to retrieve the order dependence on frequency that allows to obtain a beamformer with a fixed mainlobe width over a certain frequency range. The application on simulated data shows that this result is accomplished. In fact, with a single point source, the mainlobe has constant extension for the whole frequency range considered. In presence of multiple sources, also the capability of source separation is noticeably increased with respect to Conventional Beamforming for a wide frequency range. The application of this approach to real wind tunnel experiments shows that the order tuning is able to counteract the typical increment of mainlobe width towards lower frequency. Therefore, the variation of spatial resolution across the frequency is considerably reduced. In experimental applications, this approach may be limited by the highest order allowed, depending on the array calibration and steering vector accuracy. Anyway, it is possible to apply this method to a wide frequency range by splitting the whole range of interest in different sub-ranges. For each of them, different target mainlobe width can be chosen in order to limit the maximum order. Further analysis should be carried out on the variability of order-frequency dependence with respect to the target source position, array design and other parameters. Despite the effectiveness of the tuning procedure presented in this paper, another aspect to investigate is the residual behaviour of the mainlobe radius dependence on ν and frequency, and how to take into account of it in the tuning process.

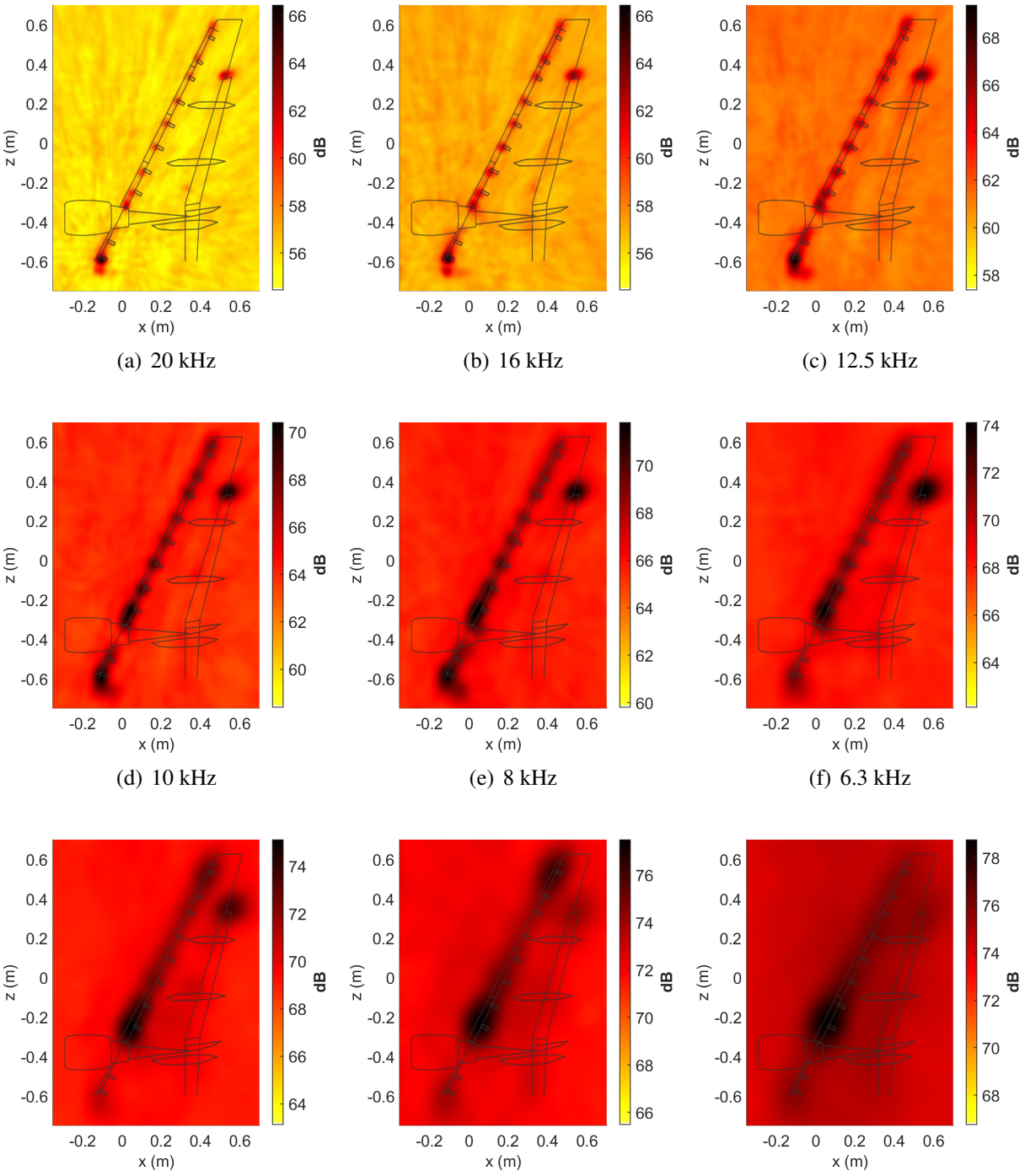

(a) 20 kHz (b) 16 kHz (c) 12.5 kHz

(d) 10 kHz (e) 8 kHz (f) 6.3 kHz

(g) 5 kHz (h) 4 kHz (i) 3.15 kHz

Figure 13: DLR1 benchmark data. Acoustic maps for different one-third octave bands with Conventional Beamforming.

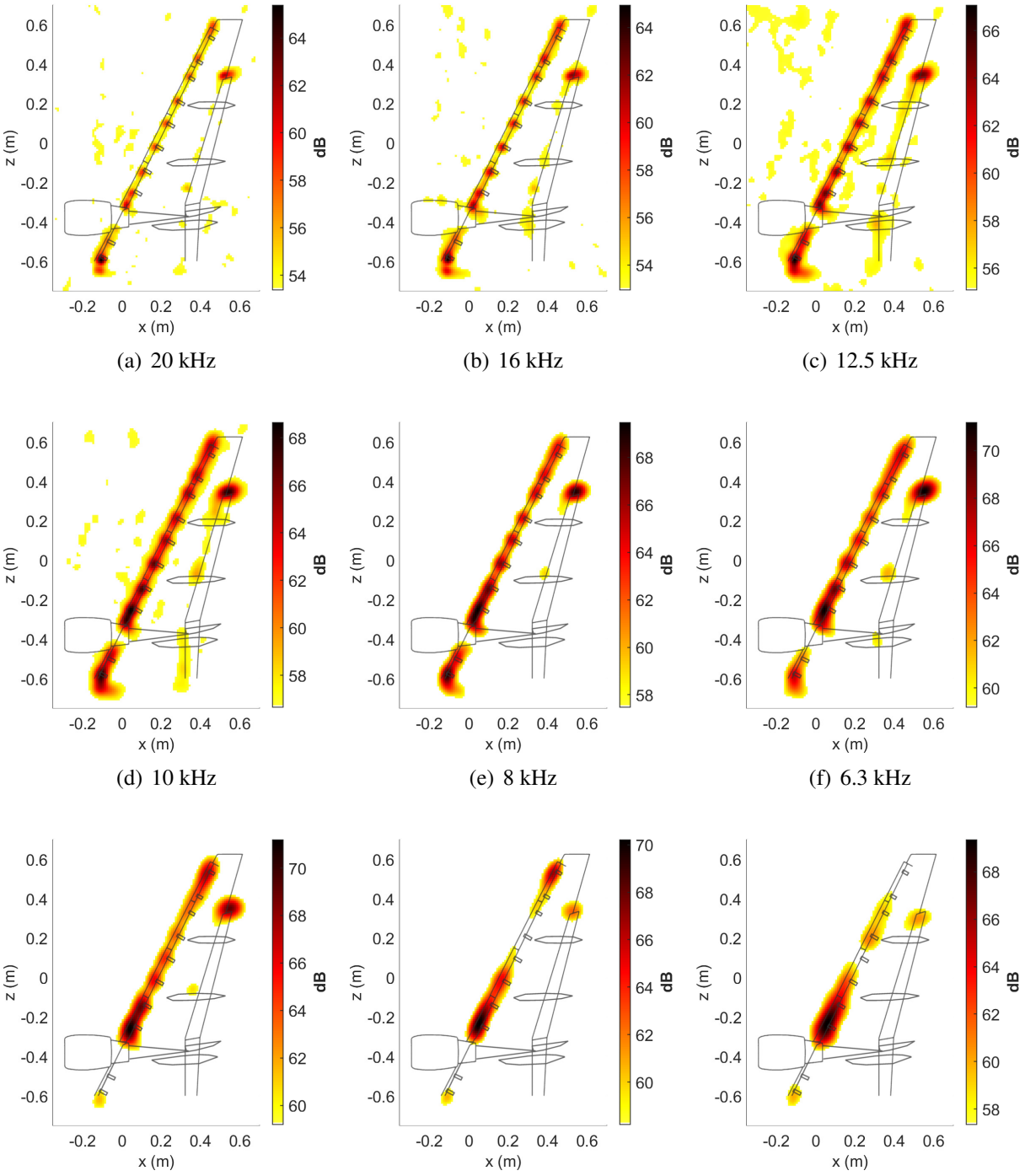

(a) 20 kHz (b) 16 kHz (c) 12.5 kHz

(d) 10 kHz (e) 8 kHz (f) 6.3 kHz

(g) 5 kHz (h) 4 kHz (i) 3.15 kHz

Figure 14: DLR1 benchmark data. Acoustic maps for different one-third octave bands with Functional Beamforming and tuned order $\bar{\nu}$ ($He_{tgt} = 80$, $K = 2.0288$).

REFERENCES

[1] T. Ahlefeldt. "Aeroacoustic measurements of a scaled half-model at high reynolds numbers." *AIAA Journal*, 51(12), 2783–2791, 2013. doi:10.2514/1.J052345. URL https://doi.org/10.2514/1.J052345.

[2] T. Ahlefeldt. "Array methods hdf5-benchmark data.", 2022. URL https://www.b-tu.de/fg-akustik/lehre/aktuelles/arraybenchmark, maintained by Thomas Geyer.

[3] O. Amoiridis, R. Zamponi, A. Zarri, J. Christophe, and C. Schram. "Localization and characterization of rotating noise sources on axial fans by means of an irregularly shaped microphone array." *Journal of Physics: Conference Series*, 1909(1), 012003, 2021. doi:10.1088/1742-6596/1909/1/012003.

[4] Bahr and Lockard. "Designing shading schemes for microphone phased arrays." In *Proceedings on CD of the 8th Berlin Beamforming Conference, March 2-3, 2020*. GFaI, Gesellschaft zu Förderung angewandter Informatik e.V., Berlin, 2020. URL https://www.bebec.eu/fileadmin/bebec/downloads/bebec-2020/papers/BeBeC-2020-S01.pdf.

[5] Baron, Finez, and Nicolas. "Numerical and experimental assessment of functional beamforming for source quantification." In *Proceedings on CD of the 7th Berlin Beamforming Conference, March 5-6, 2018*. GFaI, Gesellschaft zu Förderung angewandter Informatik e.V., Berlin, 2018. ISBN 978-3-942709-20-0. URL http://www.bebec.eu/Downloads/BeBeC2018/Papers/BeBeC-2018-S08.pdf.

[6] G. Battista, P. Chiariotti, and P. Castellini. "Spherical harmonics decomposition in inverse acoustic methods involving spherical arrays." *Journal of Sound and Vibration*, 433, 425–460, 2018. doi:10.1016/j.jsv.2018.05.001.

[7] G. Battista, P. Chiariotti, M. Martarelli, and P. Castellini. "Inverse methods in aeroacoustic three-dimensional volumetric noise source localization and quantification." *Journal of Sound and Vibration*, 473, 115208, 2020. doi:10.1016/j.jsv.2020.115208.

[8] G. Battista, G. Herold, E. Sarradj, P. Castellini, and P. Chiariotti. "IRLS based inverse methods tailored to volumetric acoustic source mapping." *Applied Acoustics*, 172, 107599, 2021. doi:10.1016/j.apacoust.2020.107599.

[9] G. Battista, M. Vanali, P. Chiariotti, and P. Castellini. "A comparison between aeroacoustic source mapping techniques for the characterisation of wind turbine blade models with microphone arrays." *ACTA IMEKO*, 10(4), 147, 2021. doi:10.21014/acta_imeko.v10i4.1142.

[10] P. Chiariotti, M. Martarelli, and P. Castellini. "Acoustic beamforming for noise source localization – reviews, methodology and applications." *Mechanical Systems and Signal Processing*, 120, 422–448, 2019. doi:10.1016/j.ymssp.2018.09.019.

[11] A. Dinsenmeyer, J. Antoni, Q. Leclère, and A. Pereira. "A probabilistic approach for cross-spectral matrix denoising: Benchmarking with some recent methods." *The Journal of the Acoustical Society of America*, 147(5), 3108–3123, 2020. doi:10.1121/10.0001098. URL https://doi.org/10.1121/10.0001098.

[12] Dougherty. "Functional beamforming." In *Proceedings on CD of the 5th Berlin Beamforming Conference, 19-20 February 2014*. GFaI, Gesellschaft zu Förderung angewandter Informatik e.V., Berlin, 2014. ISBN 978-3-942709-12-5. URL http://bebec.eu/Downloads/BeBeC2014/Papers/BeBeC-2014-01.pdf.

[13] L. R. F.R.S. "Xxxi. investigations in optics, with special reference to the spectroscope." *The London, Edinburgh, and Dublin Philosophical Magazine and Journal of Science*, 8(49), 261–274, 1879. doi:10.1080/14786447908639684. URL https://doi.org/10.1080/14786447908639684.

[14] J. Hald. "Removal of incoherent noise from an averaged cross-spectral matrix." *The Journal of the Acoustical Society of America*, 142(2), 846–854, 2017. doi:10.1121/1.4997923.

[15] Jekosch, Herold, and Sarradj. "Virtual rotating array methods for arbitrary microphone configurations." In *Proceedings on CD of the 8th Berlin Beamforming Conference, March 2-3, 2020*. GFaI, Gesellschaft zu Förderung angewandter Informatik e.V., Berlin, 2020. URL https://www.bebec.eu/fileadmin/bebec/downloads/bebec-2020/papers/BeBeC-2020-D10.pdf.

[16] S. Jekosch and E. Sarradj. "An inverse microphone array method for the estimation of a rotating source directivity." *Acoustics*, 3(3), 462–472, 2021. doi:10.3390/acoustics3030030.

[17] Leclere, Perreira, Bailly, Antoni, and Picard. "A unified formalism for acoustic imaging techniques: Illustrations in the frame of a didactic numerical benchmark." In *Proceedings on CD of the 6th Berlin Beamforming Conference, 29 February - 1 March 2016*. GFaI, Gesellschaft zu Förderung angewandter Informatik e.V., Berlin, 2016. ISBN 978-3-94270915-6. URL http://www.bebec.eu/Downloads/BeBeC2016/Papers/BeBeC-2016-D5.pdf.

[18] R. Merino-Martínez, P. Sijtsma, M. Snellen, T. Ahlefeldt, J. Antoni, C. J. Bahr, D. Blacodon, D. Ernst, A. Finez, S. Funke, T. F. Geyer, S. Haxter, G. Herold, X. Huang, W. M. Humphreys, Q. Leclère, A. Malgoezar, U. Michel, T. Padois, A. Pereira, C. Picard, E. Sarradj, H. Siller, D. G. Simons, and C. Spehr. "A review of acoustic imaging methods using phased microphone arrays." *CEAS Aeronautical Journal*, 10(1), 197–230, 2019. doi:10.1007/s13272-019-00383-4.

[19] R. Merino-Martínez, M. Snellen, and D. G. Simons. "Functional beamforming applied to imaging of flyover noise on landing aircraft." *Journal of Aircraft*, 53(6), 1830–1843, 2016. doi:10.2514/1.c033691.

[20] C. Ocker, E. Blumendeller, P. Berlinger, W. Pannert, and A. Clifton. "Localization of wind turbine noise using a microphone array in wind tunnel measurements." *Wind Energy*, 25(1), 149–167, 2021. doi:10.1002/we.2665.

[21] E. Sarradj. "Three-dimensional acoustic source mapping with different beamforming steering vector formulations." *Advances in Acoustics and Vibration*, 2012, 1–12, 2012. doi:10.1155/2012/292695.

[22] P. Sijtsma. "Phased array beamforming applied to wind tunnel and fly-over tests." In *SAE Technical Paper Series*. SAE International, 2010. doi:10.4271/2010-36-0514.

[23] B. V. Veen and K. Buckley. "Beamforming: a versatile approach to spatial filtering." *IEEE ASSP Magazine*, 5(2), 4–24, 1988. doi:10.1109/53.665.

[24] P. Welch. "The use of fast fourier transform for the estimation of power spectra: A method based on time averaging over short, modified periodograms." *IEEE Transactions on Audio and Electroacoustics*, 15(2), 70–73, 1967. doi:10.1109/TAU.1967.1161901.

[25] R. Zamponi, P. Chiariotti, G. Battista, C. Schram, and P. Castellini. "3d generalized inverse beamforming in wind tunnel aeroacoustic testing: application to a counter rotating open rotor aircraft model." *Applied Acoustics*, 163, 107229, 2020. doi:10.1016/j.apacoust.2020.107229.